SPE · AAPG · SEG
CCUS
Carbon Capture, Utilization, and Storage

CCUS: 4423733

Experimental Investigation of Secondary Mineral Formation during CO_2 Basalt Interaction under Reservoir Conditions

Elizabeth Appiah*[1], Ernest Owusu[1], Jason Simmons[2], Xiaojing Ge[2], Jiyue Wu[2], Xicong Ma[1], Sai Wang[2], 1. New Mexico Institute of Mining and Technology. Petroleum Recovery Research Center.

Abstract

Carbon mineralization is a reliable mechanism for the permanent sequestration of CO_2 in basaltic formations through the formation of stable carbonate and silicate minerals. Basalt formations are exceptionally reactive CO_2 storage candidates because they favor rapid mineral–fluid reactions that promote long-term storage security. Dissolution of basaltic minerals and precipitation of secondary phases alters fluid geochemistry and potentially pore structure during CO_2 injection and storage. Secondary mineral formation is thought to alter porosity permeability and injectivity but these effects have not been well constrained. In this work, laboratory flow through experiment designed to quantify dissolution of basaltic primary minerals and conditions favorable for secondary phase formation under deep subsurface storage conditions, is presented. Basaltic core scale sample was reacted with a 70 % CO_2 saturated brine at a pressure of 210 bar and 88 ºC temperature, within a triaxial core holder at a flowrate of 0.01 ml/min. Effluent fluids were measured using ICP OES to track dissolved species. Baseline solid phase mineralogy and texture were characterized using XRD, EPMA, BET and XRCT methods. Ca^{2+}, Mg^{2+}, Fe^{2+}, Al^{3+} and SiO_2(aq)were released into solution demonstrating dissolution of basaltic primary minerals labile to CO_2 such as forsterite and anorthite. Reaction progress evolved with flow rate through variations in fluid residence time. Stabilization of Ca^{2+} concentrations and sustained suppression of dissolved Al^{3+} indicate evolving secondary controls on fluid chemistry during reaction. Petrophysical laboratory measurements indicate all runs experienced increases in permeability though porosity changes differed from different flow rates. Laboratory evidence that basalt-CO_2 interactions have the potential to evolve towards mineral trapping while altering pore structure and flow pathways is provided by this study.

Introduction

Basalt formations have emerged as promising targets for geological CO_2 storage due to abundant reactive silicate minerals and the potential to immobilize CO_2 through mineral trapping (McGrail et al., 2006;

Owusu et al., 2025). Another distinction from sedimentary reservoirs is that injected CO2 can be transformed into permanent solid mineral phases in basalt, enhancing security of storage (Matter et al., 2016; Snæbjörnsdóttir et al., 2018). Injection of CO_2 bearing fluids results in enhanced dissolution kinetics of olivine, plagioclase and pyroxene minerals releasing cations such as Ca^{2+}, Mg^{2+} and Fe^{2+} available for secondary carbonate and aluminosilicate precipitation (Gislason & Oelkers, 2014; Alfredsson et al., 2013). The implications of these secondary phases on pore structure evolution and injectivity is currently not well understood due to analytical limitations. While secondary minerals have been identified via XRD and other analytical methods, most experiments have been time-limited and HPHT conditions pose challenges for direct mineral identification (Menefee et al., 2017; Deng et al., 2025). Effluent geochemistry is therefore widely used to assess dissolution and infer secondary controls during CO_2 rock interaction (Luhmann et al., 2017; Menefee et al., 2018). Laboratory flow-through experiment was performed to study interactions between CO_2 and basalt under reservoir relevant conditions (Gilfillan et al., 2025). Effluent analysis coupled with initial characterization of the solid was used to quantify primary dissolution and determine the potential for secondary phase formation. Linking reaction conditions to evolving geochemistry in basalt provides constraints on CO_2 storage mechanisms and pathways for pore-scale evolution. Mineralogical and geo-textural baseline characteristics of the basalt core flooded in this study are summarized in Appendix Figure A1 and Figure A2.

Theory and Methods

Basalt core preparation and pre-experimental characterization

Basalt core plug (1in x 2 in) was prepared for triaxial flow through testing. Baseline mineralogical and microstructural characterization was completed before reaction to define initial conditions. XRD identified the primary crystalline phases present in the starting material including augite, forsterite and anorthite consistent with a mafic assemblage. EPMA was used to quantify representative compositions for four targeted phases, pyroxene, olivine, feldspar and glass. These baseline compositions provide constraints for interpreting dissolution signatures in the effluent chemistry and for selecting mineral endmembers in saturation index calculations. BET surface area measurements (Beckingham et al., 2016) and XRCT imaging were performed on the unreacted cores to quantify initial surface and pore structure. XRCT derived porosity was used alongside laboratory porosity measurements to track changes after testing. XRD results (Appendix Figure A1) and EPMA-guided BSE imaging (Appendix Figure A2) were used to define primary mineral phases before reaction.

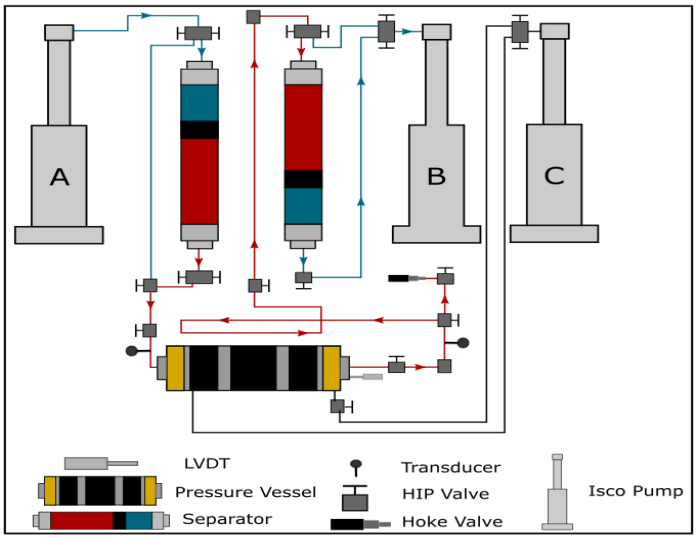

Figure 1. Schematic of the core-scale flow-through experimental system showing CO_2 saturation, brine injection, triaxial core holder, confining and pore pressure control and effluent sampling configuration. Modified from Simmons et al. (2026)

Flow-through experimental and effluent sampling

Core scale flow through experiment was conducted using a triaxial core holder and a multiple pump system to maintain confining pressure (407 bar) and pore pressure (210 bar) under reservoir relevant conditions. CO_2 saturated brine was injected at a flow rate of 0.01 ml/min, to isolate residence time effects. Effluent fluids were collected over the course of the experiment and analyzed by ICP OES. Results are reported as mmol/L for comparison across ions and flow rates. A schematic of the experimental setup is shown in Figure 1.

Geochemical interpretation using saturation indices

Saturation indices (SI) were modeled using Geochemist Workbench (Snæbjörnsdóttir et al., 2018) for representative carbonates and silicates to evaluate the potential for secondary precipitation during reactive experiments. Reported SI values are log (Q/K), where negative indicates a phase is undersaturated in solution (dissolution is the preferred geochemical reaction path), and positive indicates a phase is oversaturated in solution (thermodynamic favorability for precipitation)**.**

Results

Pre-Experimental Basalt Core Characterization

Baseline characterization confirms a reactive mafic assemblage dominated by augite, forsterite and anorthite. EPMA results indicate that olivine is Mg–Fe rich, pyroxene is Ca–Mg–Fe bearing, plagioclase is Ca–Na–Al–Si dominated, and the glass phase is enriched in Si and Al with moderate alkali content, providing a mineralogical basis for the release of Ca^{2+}, $Mg^{2+,}$ Fe^{2+}, Al^{3+} and SiO_2(aq) during CO_2 fluid-rock interaction. Baseline pore structure characterized by XRCT (Appendix Figure A12) shows a fine-grained basalt matrix with distributed intergranular and vesicular porosity. These results establish that subsequent geochemical changes reflect reactions initiated during the experiments rather than pre-existing alteration. BET adsorption–desorption isotherms indicate a reduction in accessible surface area following reaction, consistent with surface passivation and mesopore modification by secondary mineral precipitation under low flow conditions (Appendix Figure A10-11).

Effluent Geochemical Evolution and CO_2 Behavior

Effluent chemistry results for major reactive species are shown in Appendix Figure A3. Concentrations of Ca^{2+}, Mg^{2+}, $Fe^{2+,}$ Al^{3+} and dissolved silica increase rapidly at early time, indicating dissolution of labile basaltic minerals. Ca^{2+} rise sharply and then stabilize at approximately constant levels, suggesting early buffering by Ca-bearing phases or progressive loss of highly reactive Ca-rich surface sites while Mg^{2+}, Fe^{2+} and SiO_2(aq) continue to increase gradually with fluid volume, consistent with sustained dissolution of olivine and pyroxene under prolonged residence time conditions. Dissolved Al^{3+} remains low and decreases with time, indicating strong secondary control on aluminum mobility. Strontium exhibits an

early concentration peak followed by a decline toward steady values, consistent with rapid initial plagioclase dissolution and subsequent incorporation into secondary phases (Appendix Figure A4). Conservative species including Na^+, Cl^- and SO_4^{2-} remain relatively stable, confirming that reactive ion trends reflect mineral–fluid interaction rather than hydrodynamic variability (Appendix Figure A5). The concentration of CO_2 initially decreases at early reaction times due to fast consumption of CO2 reacting with dissolved basalt and buffering reactions. The dissolved CO_2 slowly rebounds towards a plateau value as the reaction progresses and larger fluid volumes become reactive. The system moves towards an apparent steady state where CO_2 supply, basalt dissolution reaction rates and changing fluid chemistry (due to long residence time) are balanced. Dissolved CO_2 concentration trend are shown in Appendix Figure A6.

Saturation index evolution and mineral stability

Saturation index evolution for representative carbonates and silicates is shown in Appendix Figures A7 to A9. Modeling of saturation indices indicates primary silicates including forsterite, anorthite, and augite remain undersaturated throughout all experiments, confirming continued basalt dissolution despite increasing dissolved Mg^{2+}, Fe^{2+}, and SiO_2(aq). Although silicate SI values increase with reaction progress, none approach equilibrium, indicating sustained reactivity of the basalt framework under low flow conditions. Carbonate phases exhibit contrasting behavior. Calcite and magnesite remain undersaturated during the experiment, although their SI values increase toward near-equilibrium conditions as reaction progresses. Opposite behavior is observed for siderite as it evolves from high undersaturation early on to saturation and eventual oversaturation towards the end of the fluid volume experiments. This behavior tracks with the near constant rise in dissolved Fe^{2+} concentrations and suggests that Fe^{2+} availability is an important factor regulating carbonate saturation state. Thus, the experiment shows that potential for carbonate precipitation is mineral dependent and closely tied to factors such as residence time and cation supply.

Petro-physical changes

Permeability increased from 4.2 to 5.0 mD over the duration of the experiment. Porosity decreased from 10% to 8.08% as determined by laboratory analysis but not shown by XRCT. The difference may indicate that dissolution increased pore interconnectivity and flow paths while localized secondary uptake or redistribution of reaction products decreased overall pore volume. These observations highlight the coexistence of dissolution-driven permeability enhancement and secondary mineral-related pore modification during CO_2–basalt interaction at long residence times.

Discussion

The experiment provides a clear view of basalt CO_2 reaction pathways under long residence time conditions (Menefee et al., 2017). The continued undersaturation with respect to primary basaltic minerals indicates that dissolution of basalt continues to be thermodynamically favorable during the experiment, providing continued supply of divalent cations available for mineral trapping (Gysi & Stefansson, 2012). Reasonable steady-state is reached for Ca^{2+} concentrations, while Mg^{2+} and Fe^{2+}continue to rise steadily. This fact along with different saturation indices for the carbonate minerals indicates different reactivity of the basaltic phases and likely changing surface areas controlling reaction rates. From variations of the saturation index during the experiment, it can be seen that not all phases will precipitate carbonate minerals to the same extent. Calcite and magnesite experience nearly no saturation upon completion of the experiments, while siderite saturates at longer reaction times due to coupled release of Fe^{2+}. Therefore, mineral trapping with iron carbonate may become more important during early times for basalt storage containing Fe-rich phases. Aluminum behavior provides important constraints on secondary reaction pathways. The sustained suppression of dissolved Al^{3+} despite ongoing silicate dissolution indicates the formation of aluminosilicate phases, which may influence pore-scale evolution even when carbonates dominate long-term trapping mechanisms. Coupling of the geochemical and petrophysical

trends indicates that dissolution and secondary precipitation are happening simultaneously, leading to a decrease in porosity while permeability is increasing (Gilfillan et al., 2025). These simultaneous reactions emphasize the importance of understanding fluid chemistry as well as pore-scale evolution during evaluation of injectivity and storage security for CO_2 storage in basalts. Identification of the post-reaction solid phase will be included in future analyses to pinpoint secondary minerals formed and measure their distribution, allowing for a closer correlation between geochemical signatures and pore-scale changes.

Conclusions

Baseline XRD and EPMA indicate a reactive assemblage comprised dominantly of augite, forsterite, anorthite and glass, providing a mineralogical framework for interpreting effluent dissolution signatures. Flow-through experiments indicate that prolonged residence time leads to sustained CO_2 basalt reactivity under storage-relevant conditions. Ca^{2+} is released rapidly and early during reaction before stabilizing; Mg^{2+}, Fe^{2+}, and SiO_2(aq) concentrations continue to increase throughout experimentation, indicating continued silicate dissolution. Dissolved Al^{3+} concentrations are suppressed throughout reaction, suggesting that aluminum mobilility is governed by strong secondary processes. Reaction path modeling via SI calculations indicates that silicate minerals never approach saturation, whereas carbonate phases progressively approach saturation throughout reaction, with iron-bearing carbonates exhibiting the greatest saturation tendencies at longer time scales. Petrophysical analyses indicate that permeability increases slightly as porosity decreases during reaction, showing that increased pore connectivity can occur in tandem with local decreases in pore volume. These results elucidate the impacts of residence time on geochemical evolution, mineral trapping potential, and pore-scale controls during CO_2 storage in basalt.

References

Alfredsson, H. A., Oelkers, E. H., Hardarsson, B. S., Franzson, H., Gunnlaugsson, E., & Gislason, S. R. (2013). The geology and water chemistry of the Hellisheidi, SW-Iceland carbon storage site. *International Journal of Greenhouse Gas Control*, *12*, 399-418. https://doi.org/10.1016/j.ijggc.2012.07.001

Beckingham, L. E., Mitnick, E. H., Steefel, C. I., Zhang, S., Voltolini, M., Swift, A. M., Yang, L., Cole, D. R., Sheets, J. M., Ajo-Franklin, J. B., DePaolo, D. J., Mito, S., & Xue, Z. (2016). Evaluation of mineral reactive surface area estimates for prediction of reactivity of a multi-mineral sediment. *Geochimica et Cosmochimica Acta, 188,* 310-329. https://doi.org/10.1016/j.gca.2016.05.040

Deng, H., Ellis, B. R., Peters, C. A., Fitts, J. P., Crandall, D., & Bromhal, G. S. (2025). Accelerated CO_2 mineralization in basalt via reaction process control: Mineralization effect, mineral evolution, and reservoir property implications. *Journal of Geoscience and Environment Protection*, *13*(1), 205648. https://doi.org/10.1016/j.jgsce.2025.205648

Gilfillan, S. M. V., Wild, B., Marzoli, A., Minardi, A., Pellegrino, S., & Benson, S. M. (2025). Changes in permeability and pore structure induced by CO_2-water-basalt interaction: Insights from flow-through experiments at 200°C. *Journal of Geophysical Research: Solid Earth*, *130*(1), e2025JB031141. https://doi.org/10.1029/2025JB031141

Gislason, S. R., & Oelkers, E. H. (2014). Carbon storage in basalt. *Science*, *344*(6182), 373–374. https://doi.org/10.1126/science.1250828

Gysi, A. P., & Stefánsson, A. (2012). CO_2-water-basalt interaction. Numerical simulation of low temperature CO_2 sequestration into basalts. *Geochimica et Cosmochimica Acta, 81*, 129-152. https://doi.org/10.1016/j.gca.2011.12.012

Luhmann, A. J., Tutolo, B. M., Bagley, B. C., Mildner, D. F. R., Seyfried, W. E., & Seyfried, M. O. (2017). Whole rock basalt alteration from CO_2-rich brine during flow-through experiments at 150°C and 150 bar. *Chemical Geology*, *453*, 92-110. https://doi.org/10.1016/j.chemgeo.2017.02.002

Matter, J. M., Stute, M., Snæbjörnsdóttir, S. Ó., Oelkers, E. H., Gislason, S. R., Aradottir, E. S., Sigfusson, B., Gunnarsson, I., Sigurdardottir, H., Gunnlaugsson, E., Axelsson, G., Alfredsson, H. A., Wolff-Boenisch, D., Mesfin, K., Taya, D. F. de la R., Hall, J., Dideriksen, K., & Broecker, W. S. (2016). Rapid carbon mineralization for permanent disposal of anthropogenic carbon dioxide emissions. *Science*, *352*(6291), 1312–1314. https://doi.org/10.1126/science.aad8132

McGrail, B. P., Schaef, H. T., Ho, A. M., Chien, Y.-J., Dooley, J. J., & Davidson, C. L. (2006). Potential for carbon dioxide sequestration in flood basalts. *Journal of Geophysical Research: Solid Earth*, *111*(B12), B12201. https://doi.org/10.1029/2005JB004169

Menefee, A. H., Li, P., Giammar, D. E., & Ellis, B. R. (2017). Roles of transport limitations and mineral heterogeneity in carbonation of fractured basalts. *Environmental Science & Technology, 51*(18), 9352-9362. https://doi.org/10.1021/acs.est.7b00326

Menefee, A. H., Giammar, D. E., & Ellis, B. R. (2018). Permanent CO_2 trapping through localized and chemical gradient-driven basalt carbonation. *Environmental Science & Technology, 52*(15), 8954-8964. https://doi.org/10.1021/acs.est.8b01814

Owusu, E. A., Wu, J., Appiah, E. A., Marfo, W. A., Yuan, N., Ge, X., Wang, S., Simmons, J., & Ma, X. (2025). Carbon mineralization in basaltic rocks: Mechanisms, applications, and prospects for permanent CO_2 sequestration. *Energies*, *18*(13), 3489. https://doi.org/10.3390/en18133489

Simmons et al., (2026). Hydrogeochemical control on mean-stress dependent permeability and mechanical response in eolian sandstone during reaction with CO2-enriched fluid. (In review)

Snæbjörnsdóttir, S. Ó., Gislason, S. R., Galeczka, I. M., & Oelkers, E. H. (2018). Reaction path modelling of in-situ mineralisation of CO_2 at the CarbFix site at Hellisheidi, SW-Iceland. *Geochimica et Cosmochimica Acta, 220*, 348-366. https://doi.org/10.1016/j.gca.2017.09.053

Appendix

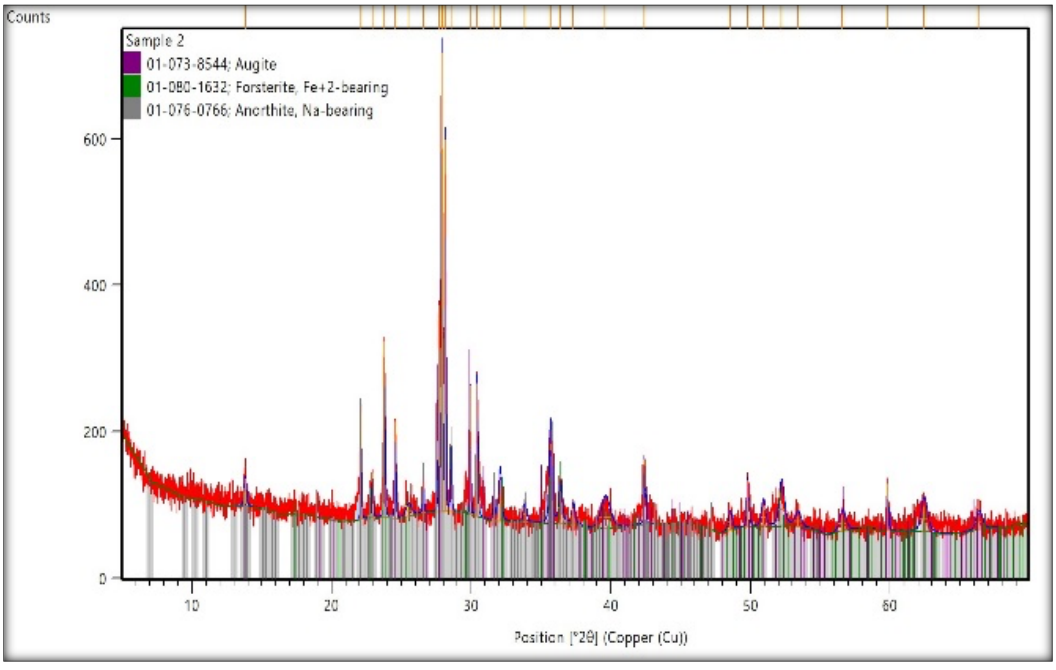

Figure A- 1. . Schematic of the core-scale flow-through experimental system showing CO_2 saturation, brine injection, triaxial core holder, confining and pore pressure control and effluent sampling configuration. Modified from Simmons et al. (2026)

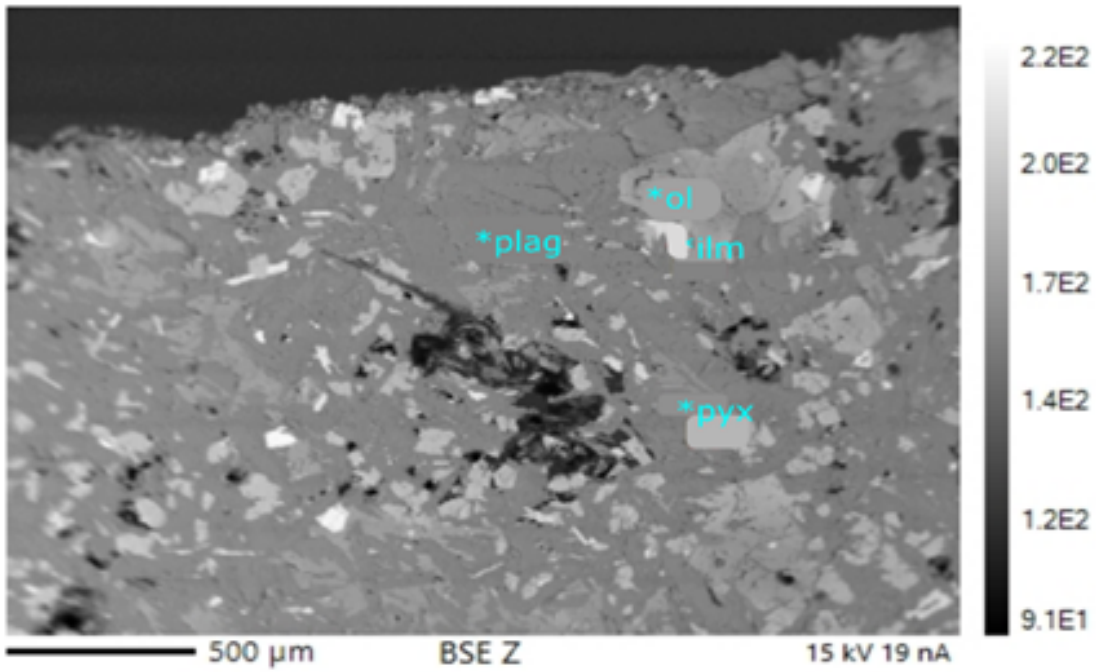

Figure A- 2. . Representative backscattered electron (BSE) image of the unreacted basalt illustrating heterogeneous texture and distribution of primary phases including plagioclase (plag), olivine (ol), pyroxene (pyx) and opaque minerals.

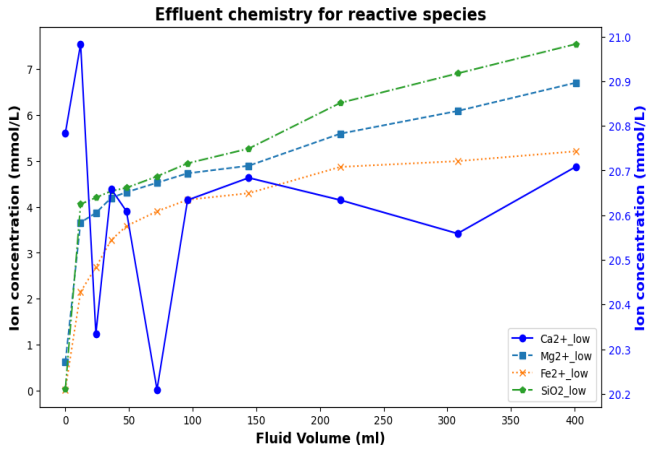

Figure A- 3. Time-resolved effluent concentrations of major reactive species Ca^{2+}, Mg^{2+}, Fe^{2+}, and SiO_2(aq) during flow-through experiments at a flow rate of 0.01 mL/min.

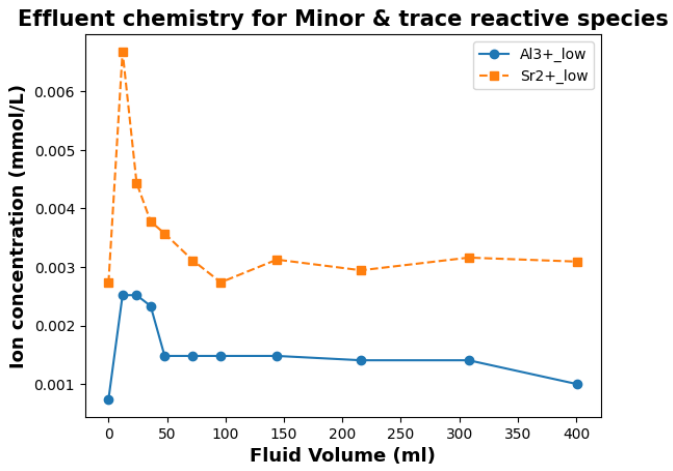

Figure A- 4. Time-resolved effluent concentrations of minor and trace reactive species Al^{3+} and Sr^{2+} during flow-through experiments at a flow rate of 0.01 mL/min.

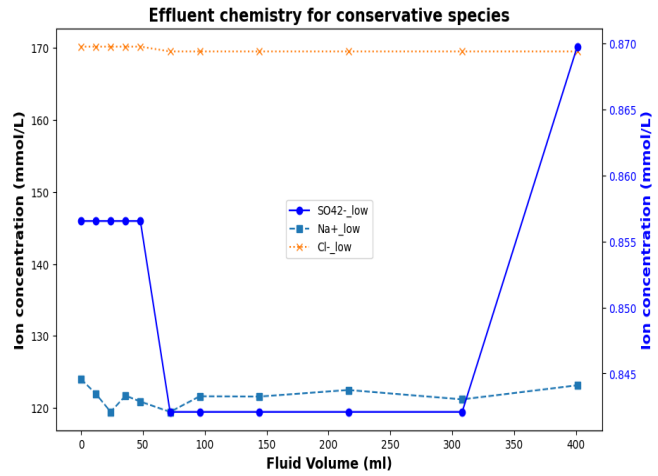

Figure A- 5. Time-resolved effluent concentrations of conservative species Cl^-, Na^+, and SO_4^{2-} during flow-through experiments at a flow rate of 0.01 mL/min.

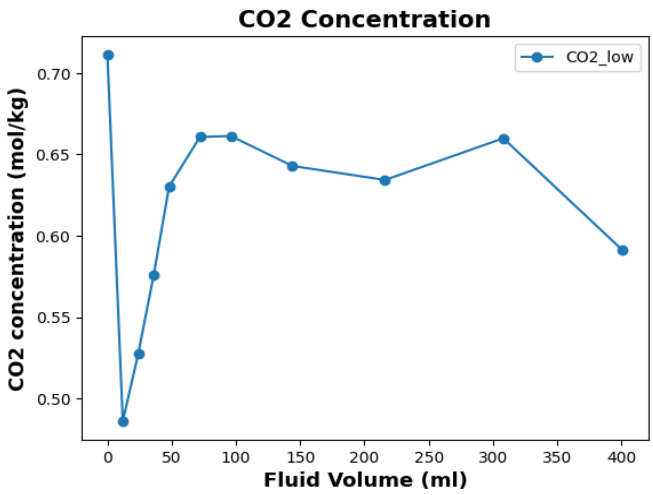

Figure A- 6. Evolution of dissolved CO_2 concentration during flow-through experiments at a flow rate of 0.01 mL/min.

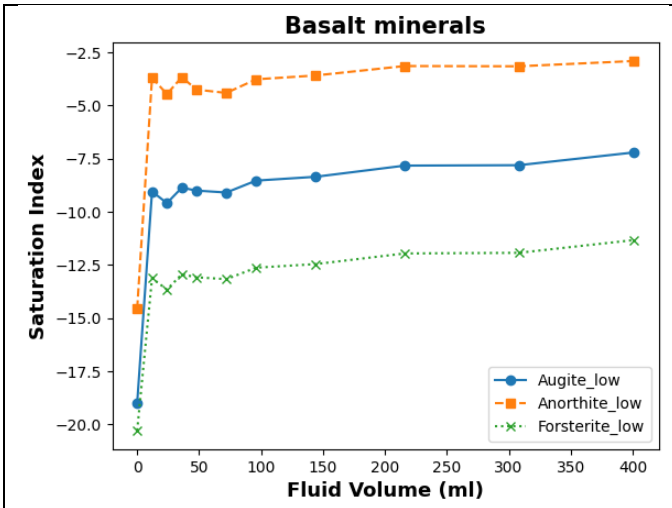

Figure A- 7. Saturation index evolution for primary silicate minerals (forsterite, anorthite, and augite) during flow-through experiments at a flow rate of 0.01 mL/min.

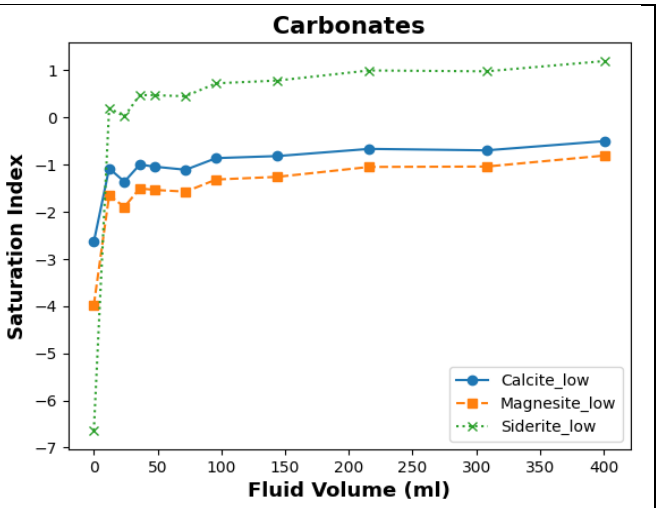

Figure A- 8. Saturation index evolution for representative carbonate minerals (calcite, magnesite, and siderite) during flow-through experiments at a flow rate of 0.01 mL/min.

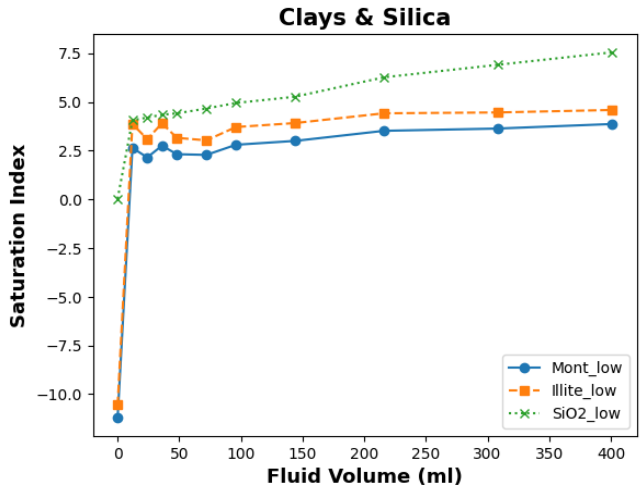

Figure A- 9. Saturation index evolution for clay minerals and silica during flow-through experiments at a flow rate of 0.01 mL/min.

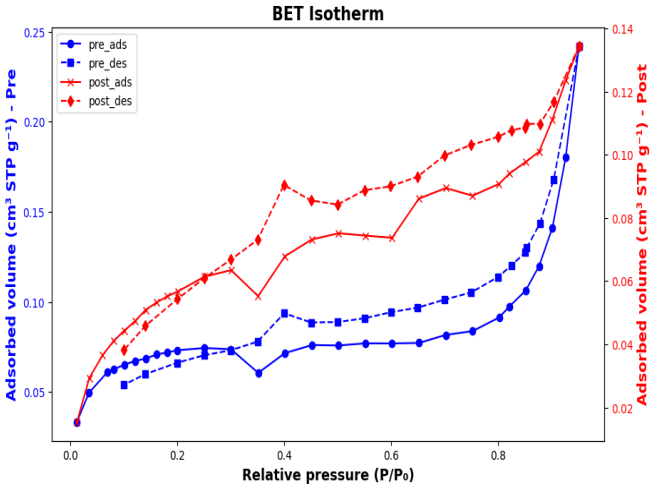

Figure A- 10. Nitrogen BET adsorption–desorption isotherms for thr basalt core measured before and after CO_2–brine reaction, illustrating changes in accessible surface area and mesoporous behavior

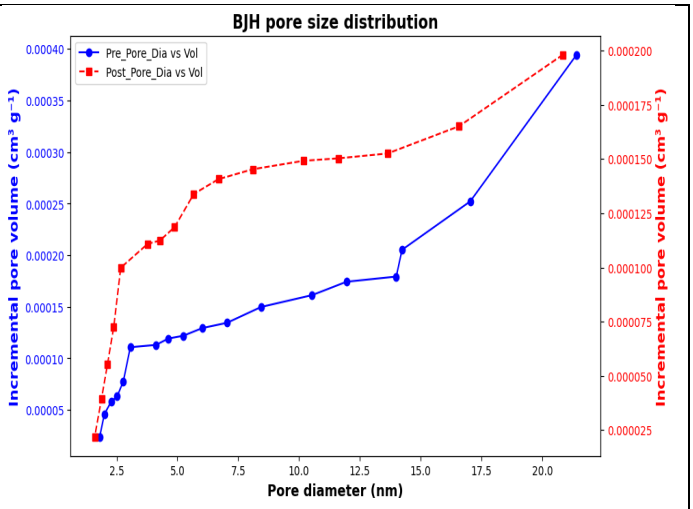

Figure A- 11. . BJH pore size distributions derived from the desorption branch of nitrogen adsorption isotherms for the basalt core before and after CO_2–brine reaction.

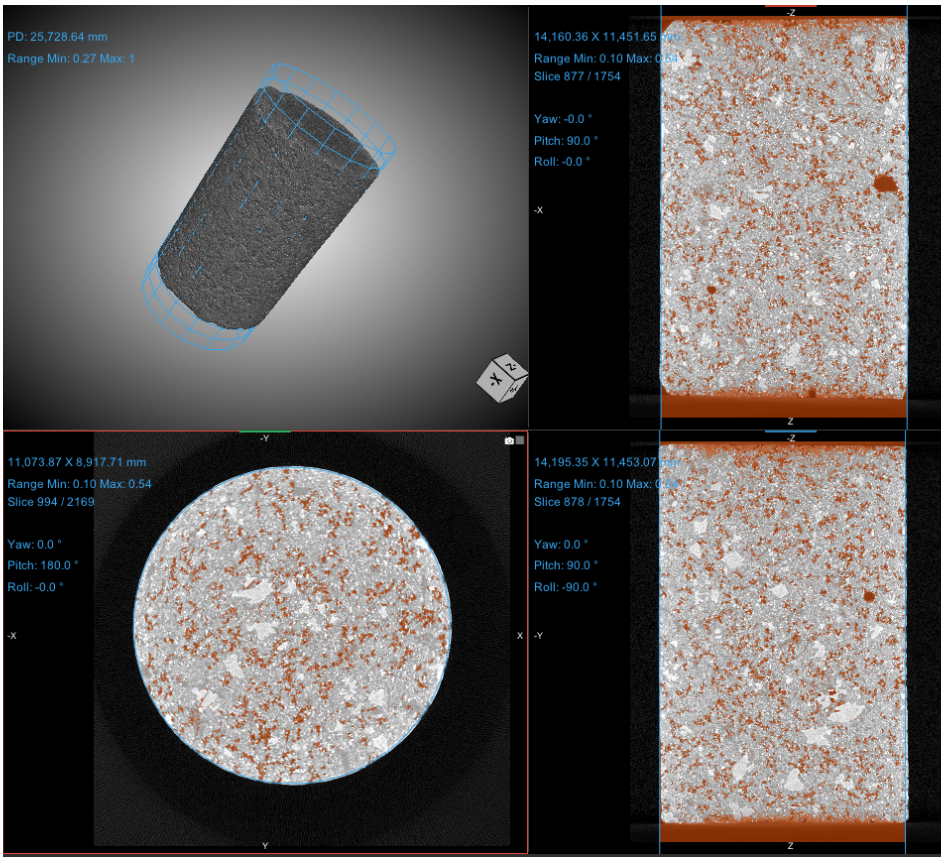

Figure A- 12. X-ray computed tomography (XRCT) images of the unreacted ABQ1 basalt core showing a fine-grained matrix with distributed intergranular and vesicular porosity in axial and transverse views.